Jets from Neutron-Star Merger Remnants and Massive Blue Kilonovae

Luciano Combi[1,2,3] and Daniel M. Siegel[4,1,2]
[1]Perimeter Institute for Theoretical Physics, Waterloo, Ontario N2L 2Y5, Canada
[2]Department of Physics, University of Guelph, Guelph, Ontario N1G 2W1, Canada
[3]Instituto Argentino de Radioastronomía (IAR, CCT La Plata, CONICET/CIC), C.C.5, (1984) Villa Elisa, Buenos Aires, Argentina
[4]Institute of Physics, University of Greifswald, D-17489 Greifswald, Germany

(Received 11 March 2023; revised 27 September 2023; accepted 14 November 2023; published 8 December 2023)

We perform three-dimensional general-relativistic magnetohydrodynamic simulations with weak interactions of binary neutron-star (BNS) mergers resulting in a long-lived remnant neutron star, with properties typical of galactic BNS and consistent with those inferred for the first observed BNS merger GW170817. We demonstrate self-consistently that within $\lesssim$30 ms postmerger magnetized ($\sigma \sim 5$–10) incipient jets emerge with asymptotic Lorentz factor $\Gamma \sim 5$–10, which successfully break out from the merger debris within $\lesssim$20 ms. A fast ($v \lesssim 0.6c$), magnetized ($\sigma \sim 0.1$) wind surrounds the jet core and generates a UV/blue kilonova precursor on timescales of hours, similar to the precursor signal due to free neutron decay in fast dynamical ejecta. Postmerger ejecta are quickly dominated by magnetohydrodynamically driven outflows from an accretion disk. We demonstrate that, within only 50 ms postmerger, $\gtrsim 2 \times 10^{-2} M_\odot$ of lanthanide-free, quasispherical ejecta with velocities $\sim$0.1–0.2c is launched, yielding a kilonova signal consistent with GW170817 on timescales of $\lesssim$5 d.

DOI: 10.1103/PhysRevLett.131.231402

Introduction.—The astrophysical origin of about half of the elements heavier than iron, created via rapid neutron capture (the *r* process), remains an open question [1,2]. The first observed binary neutron-star (BNS) merger, detected via gravitational waves [3] (GW170817), was followed by quasithermal emission [4–6] consistent with radioactive heating from the nucleosynthesis of *r*-process elements in the merger debris—a kilonova [7]. Based on inferred event rates of BNS mergers and the ejecta yield as well as the photometric and spectroscopic properties [8–15], this transient provided strong evidence not only for the production of both light (atomic mass number $A \lesssim 135$) and heavy (lanthanide-bearing; $A \gtrsim 136$) *r*-process elements in this particular event, but also for BNS mergers being a potentially dominant production site of *r*-process elements in the Universe.

Whereas the origin of the lanthanide-bearing red emission of the GW170817 kilonova peaking on timescales of a week is naturally explained by magnetohydrodynamically (MHD) driven outflows from a massive, self-regulated, neutrino-cooled accretion disk around a final remnant black hole [9,16–19], the origin of the early (∼day) blue and ultraviolet (UV) emission remained more elusive. Both the blue and red GW170817 kilonova emission are difficult to explain by dynamical debris from the collision itself [20–22] (but see Ref. [23] for a corner case). Several alternative mechanisms for the origin of the blue emission postmerger have been considered, including a combination of magnetically driven and neutrino-driven winds from a remnant NS [24–26], additional turbulent viscosity in the remnant NS [27,28], spiral waves driven into a postmerger accretion disk by nonaxisymmetric modes of a remnant NS [29], and outflows from a postmerger accretion disk both around a remnant NS [30] and a black hole [31].

Here, we demonstrate by means of self-consistent *ab initio* simulations of the merger and postmerger phases that the inferred properties of the blue GW170817 kilonova emission can arise naturally from mass ejection within only $\lesssim$50 ms postmerger due to MHD-driven winds from an accretion disk, aided by nonlinear hydrodynamic effects. The emergence of a jet from the remnant NS generates a UV/blue precursor signal and, upon collapse of the remnant, might "seed" an ultrarelativistic jet to generate a short gamma-ray burst.

Computational setup.—We solve Einstein's equations coupled to the general-relativistic magnetohydrodynamic equations with weak interactions using an enhanced version [32,33] of the flux-conservative code GRHydro [34,35], which is part of the EINSTEINTOOLKIT [36] open-source code framework [37–41]. We use the numerical setup in Ref. [33] (henceforth CS23) with an atmosphere floor of $\rho_{\rm atm} \sim 5 \times 10^2$ g cm^{-3}. We implement the recovery of primitive variables in Ref. [42], which provides support for tabulated nuclear equations of state (EOS), weak interactions, and neutrino radiation via a one-moment approximation of the general-relativistic Boltzmann equation supplemented by a leakage scheme [43,44]. A fixed Cartesian grid hierarchy composed of six nested refinement boxes is used. The finest mesh covers $\simeq$76 km in diameter with a resolution of $\Delta x = 180$ m. The largest box has an

extend of 3000 km. Reflection symmetry across the orbital plane is employed for computational efficiency. A comparison run without imposing the symmetry at slightly lower resolution shows that our conclusions are not affected by this setup (see CS23).

The initial data consist of two cold, β-equilibrated, equal-mass NSs of radius 11.6 km and mass $1.35M_\odot$ in quasicircular orbit at a separation of 45 km. We build initial data with the elliptical solver LORENE [45], employing the Akmal-Pandharipande-Ravenhall (APR) EOS [46] in finite-temperature, tabulated form [47]. This EOS generates cold nonrotating NSs with a maximum mass of $2.2M_\odot$ and a radius of 11.6 km for a $1.4M_\odot$ NS, within the ballpark of current constraints [48,49]. While similar postmerger phenomenology is observed for the other, stiffer EOS configurations of CS23, we focus here on the APR configuration, which results in the longest-lived remnant NS. After setting the hydrodynamical variables, we initialize a weak poloidal magnetic seed field confined to the interior of each star with maximum strength of $B_{\max} = 3 \times 10^{15}$ G at the center and total energy of 10^{48} erg. The initial magnetic field is energetically and dynamically insignificant.

Magnetic field evolution and jet formation.—During inspiral, the magnetic seed field remains buried inside the stars. Starting at the merger (referred to as $t = 0$ ms), the field is amplified exponentially by the Kelvin-Helmholtz instability (KHI) [50–53] for $\approx$2 ms, as evidenced by the toroidal field in Fig. 1. Since the KHI has no characteristic spatial scale, the finite resolution of our simulation is able to capture only partial amplification of the average toroidal magnetic field from essentially 0 G to $\approx 5 \times 10^{15}$ G. In the first 15 ms postmerger, the generation of large-scale eddies in the remnant NS's interior by quasiradial core bounces further amplifies the toroidal field by an order of magnitude and roughly $\propto t^2$. These currents are associated with the formation of vortices around the inner core [54–56] which dissipate kinetic into magnetic energy.

The toroidal field eventually continues to grow at the expected linear growth rate of magnetic winding due to differential rotation inside the remnant NS. Amplification proceeds mainly in the slowly rotating core with positive angular velocity gradient interior to $r \approx 8$ km. At larger radii, a nearly rotationally supported "Keplerian envelope" is established that gradually transitions into an accretion disk formed by merger debris, a well-established quasiuniversal configuration [54,56–58]. Higher resolution would lead to earlier saturation of the turbulent magnetic field via the KHI [59–61], making the subsequent amplification processes obsolete but unlikely altering the qualitative evolution of the system.

At $\approx$25 ms after merger, thanks to magnetic winding providing an inverse turbulent cascade, the small-scale, turbulent field has been wound up into a large-scale toroidal

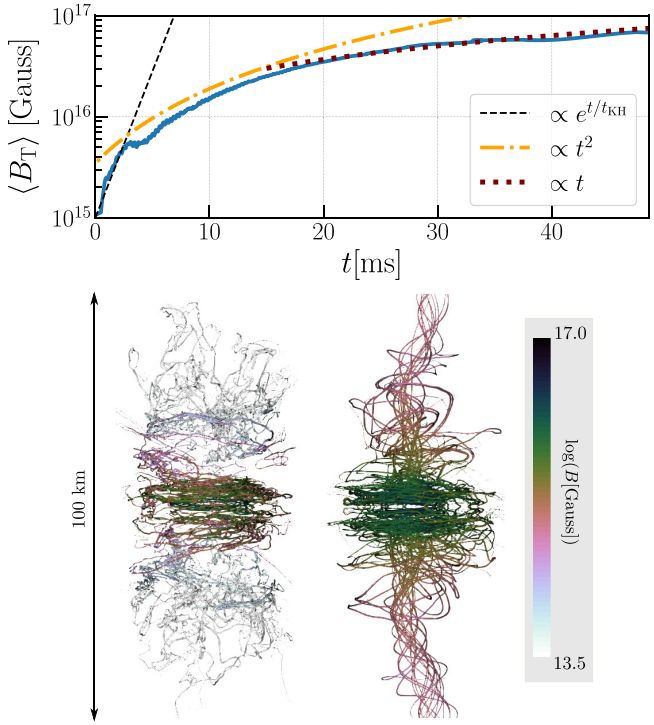

FIG. 1. Top: average toroidal field in the remnant NS as a function of time after merger (blue solid line). The dashed line represents the expected amplification by the Kelvin-Helmholtz instability, the dot-dashed line the turbulent amplification by large-scale vortices, and the dotted line the expected linear growth by magnetic winding. Bottom: 3D rendering of magnetic field lines at 15 (left) and 50 ms (right), showing the conversion of turbulent fields into large-scale toroidal structures that give rise to twin jets.

structure (Fig. 1). Owing to their magnetic buoyancy, toroidal fields eventually rise to the stellar surface in the polar regions, break out of the remnant NS, and form a magnetic tower [62] (Figs. 1 and 2).

Outflow properties.—Prior to the emergence of the magnetic tower structure, strong neutrino radiation ($L_{\nu_e} \approx 1.7 \times 10^{52}$ erg s^{-1}) from the hot merger remnant drives a neutrino-driven wind [63–65] of unbound material in polar regions with typical velocities $v \lesssim 0.1c$ and electron fraction $Y_e \approx 0.5$ via absorption of neutrinos in a gain layer above the stellar surface that extends out to $\lesssim$50 km (Fig. 2). In this gain layer, which is similar to that above proto-NSs in core-collapse supernovae, the net absorbed energy per unit time as seen by the Eulerian observer $\dot{Q}_{\rm net} = \int_{\theta<30^\circ} \dot{q}_{\rm net} \rho \Gamma \sqrt{\gamma} d^3x$ in a polar volume (polar angle $\theta < 30^\circ$) roughly equals the kinetic power $\dot{E}_k = \int_{\theta<30^\circ} \sqrt{\gamma} h \rho \Gamma (\alpha v^i - \beta^i) dA_i$ of the wind leaving that volume along the polar axis. Here, $\dot{q}_{\rm net}$ is the net specific neutrino heating rate, h is the specific enthalpy, $\Gamma = -n_\mu u^\mu$ is the Lorentz factor of the plasma with three-velocity v^i and four-velocity u^μ, dA_i is the surface element, and α, $\boldsymbol{\beta}$, and γ denote the lapse, shift, and determinant, respectively,

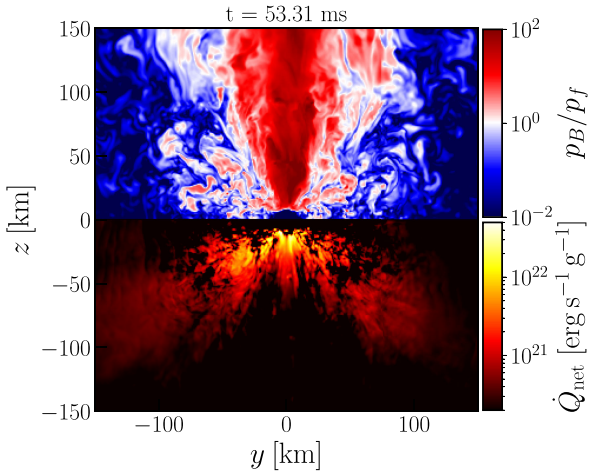

FIG. 2. Meridional snapshot showing the magnetic-to-fluid pressure ratio (upper half-plane) and the net specific neutrino heating rate (lower half-plane) once a stationary jet structure has emerged.

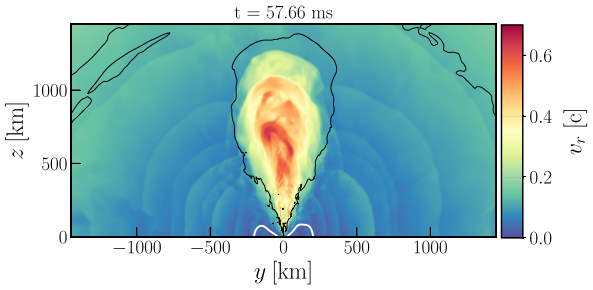

FIG. 3. Meridional snapshot of radial velocity showing the successful breakout of a high-velocity, high-entropy jet structure from the surrounding merger debris (dynamical and postmerger wind ejecta; see Supplemental Material [67]). The white contour contains bound material according to the Bernoulli criterion (the accretion disk). Black contours contain dynamically unbound ejecta (geodesic criterion). The rest of the outflow domain is unbound according to the Bernoulli criterion.

of the three-metric of the adopted $3+1$ foliation of spacetime with normal vector n^ν that defines the Eulerian observer. A steady-state wind profile $\rho \propto r^{-2}$ emerges in polar regions, as expected from mass conservation, $\dot{M} = \Delta\Omega r^2 \rho \Gamma v$, for a wind opening solid angle $\Delta\Omega$, constant mass-loss rate $\dot{M}$, and four-velocity Γv set by neutrino absorption at the base of the wind.

As the buoyant toroidal magnetic field structures break out of the remnant NS and neutrino absorption helps to form a magnetic tower along the rotational axis, a strongly magnetically dominated outflow with magnetic-to-fluid pressure ratio $p_B/p_f \approx 10^2$ is established (Fig. 2). A steady-state wind profile $\rho \propto r^{-2}$ quickly emerges (Fig. 2), with a steady-state mass-loss rate $\dot{M}$ enhanced by roughly one order of magnitude—consistent with the wind solutions in Ref. [24]. Within the same time window of 5–10 ms, the kinetic power of the outflow increases by more than an order of magnitude and comes into equipartition with neutrino heating and the (dominant) Poynting luminosity of the magnetic structure, $\dot{E}_k \approx \dot{Q}_{\rm net} + L_{\rm EM} \approx L_{\rm EM}$. The magnetization $\sigma = L_{\rm EM}/\dot{M}$ in the polar region ($\theta \lesssim 30°$ or specific entropy $s > 25 k_B$ baryon^{-1}) rapidly increases to $\sigma \approx 0.1$ (Fig. 4). Through strong neutrino heating at the base, shock heating at the jet head, and in internal shocks, the plasma outflow attains high specific entropy $\gtrsim (25\text{–}100) k_B$ baryon^{-1}. Magnetocentrifugal forces accelerate the plasma in the polar funnel from average velocities of $v \lesssim 0.1c$ (neutrino-driven wind) to $v \approx (0.25\text{–}0.6)c$. For acceleration of the wind primarily by magnetic fields, the flow should acquire a four-velocity $u = v^r \Gamma \approx c\sigma^{1/3}$ when it reaches the fast magnetosonic surface [66]. This limit with the density-averaged value of $\langle u \rangle \approx 0.35c$ is indeed reached in the polar region (Fig. 4).

A magnetized ($\sigma \sim 5\text{–}10$) jet structure emerges in the polar funnel consisting of exclusively dynamically unbound material (geodesic criterion; $-u_0 < 1$) with a half-opening angle of $\approx 20°$ and high entropy, $s \gtrsim 50 k_B$ baryon^{-1}. The jet head propagates with $v \gtrsim 0.6c$ through and breaks out from the envelope of merger debris (Fig. 3, Supplemental Material [67]). The jet is stabilized by subdominant toroidal magnetic fields in the core, which reduce instabilities at the jet-envelope boundary layer [68] while avoiding global (kink) instabilities that can develop in strongly magnetized jets ($\sigma \gg 1$) [69]. The terminal velocity of the jet outflow can be further boosted by neutrino pair annihilation (expected to be subdominant; not included here) and dissipation of magnetic and thermal energy into kinetic energy at larger spatial scales, up to $\Gamma \lesssim -u_0(h/h_\infty + b^2/\rho) \approx 5\text{–}10$. Here, h_∞ denotes the EOS-specific asymptotic value of h, and b is the comoving magnetic field strength.

During the first 50 ms postmerger, the system ejects $\gtrsim 2 \times 10^{-2} M_\odot$ of matter at a time-averaged rate of $\dot{M} \sim 0.5 M_\odot$ s^{-1}. We quantify unbound ejecta as matter at radii > 300 km using the Bernoulli criterion $-(h/h_\infty)u_0 > 1$, where h_∞ includes the approximate average binding energy of the nuclei formed by the r process [27,70]. Before the emergence of the jet structure ($t \lesssim 30$ ms), spiral waves propagating outward in the accretion disk [29,71] dominate angular momentum transport and mass ejection of the system of $\lesssim 1 \times 10^{-2} M_\odot$ with mass-averaged velocity $\langle v \rangle \approx 0.1c$. These waves and associated mass ejection, generated mainly by $m = 1$, 2 nonaxisymmetric density modes of the remnant NS through hydrodynamical instabilities [72–74], are visible as concentric waves in the radial velocity (Fig. 3), paralleled by oscillations of the unbound mass flux (Fig. 4). As the vicinity of the remnant NS becomes strongly magnetized and the jet structure emerges ($t \approx 30$ ms), the unbound mass flux increases by an order of magnitude to $\dot{M} \approx 1 M_\odot$ s^{-1} (Fig. 4), quickly dominating the total mass unbound postmerger. Within only ≈ 15 ms,

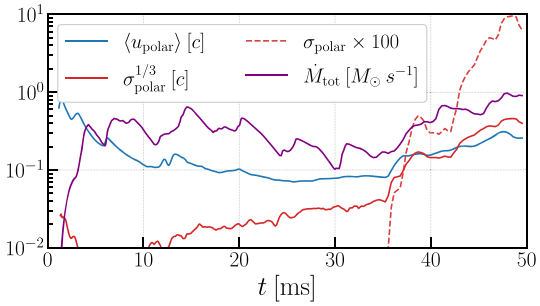

FIG. 4. Total unbound mass flux $\dot{M}_{\rm tot}$ through a spherical shell with radius 300 km and associated density-averaged local four-velocity $u = v^r\Gamma$, magnetization σ, and expected velocity at the magnetosonic surface, $\sigma^{1/3}$, in polar regions ($\theta \lesssim 30°$).

material of $\gtrsim 1\times 10^{-2}M_\odot$ ($\gtrsim$50% of the cumulative postmerger ejecta) is unbound with mass-averaged velocity $\langle v\rangle \approx 0.15c$.

As accretion blocks outward radial mass flux in equatorial regions over timescales of interest, the neutrino and magnetically driven wind from the remnant NS totaling $1\times 10^{-3}M_\odot$ escapes in polar directions ($\theta \lesssim 30°$) with only $0.2\times 10^{-3}M_\odot$ being launched within the jet core. The dominant contribution to ejected material, however, is launched as winds from the accretion disk. Disk winds intensify after ≈30 ms when angular momentum transport by spiral waves through the compact bound merger debris, magnetic stresses in the vicinity of the remnant NS, and the onset of MHD turbulence driven by the magnetorotational instability have established and enlarged the accretion disk to a radius of ≳150 km with approximate inflow-outflow equilibrium. The onset of strongly enhanced disk winds also coincides with the first cycles of an emerging dynamo as evident from a "butterfly diagram" similar to that obtained in previous work [32] (see Supplemental Material [67]). Despite intense neutrino irradiation from the remnant, the disk then settles into a self-regulated state of moderate electron degeneracy $\mu_e/k_BT \sim 1$ [16,32], which implies high neutron richness of $Y_e \approx 0.1$–0.15 [16,75,76] (see Supplemental Material [67]). The mass-averaged Y_e of the disk indeed shifts from ≈0.25 ($t < 30$ ms) to ≈0.15 as it approaches a quasistationary state with an accretion rate of $\gtrsim 1M_\odot$ s^{-1} and mass of $\approx 0.19M_\odot$.

Nucleosynthesis and kilonova.—Figure 5 shows properties of unbound outflows at the onset of neutron capture reactions ($T \approx 5$ GK) as sampled by multiple families of $\approx 2\times 10^4$ unbound passive tracer particles injected into the simulation domain (see CS23 for details). Fast outflow speeds $> 0.2c$ are almost exclusively associated with polar outflows. Material ejected from the highly neutron-rich degenerate surface layer of the remnant NS is protonized to asymptotic values of $Y_e \approx 0.3$–0.4 due to neutrino absorption. This is lower than $Y_e \approx 0.5$ as in purely neutrino-driven winds, even in the presence of fast rotation [65], due to the accelerating nature of magnetic fields [24]. Outflows

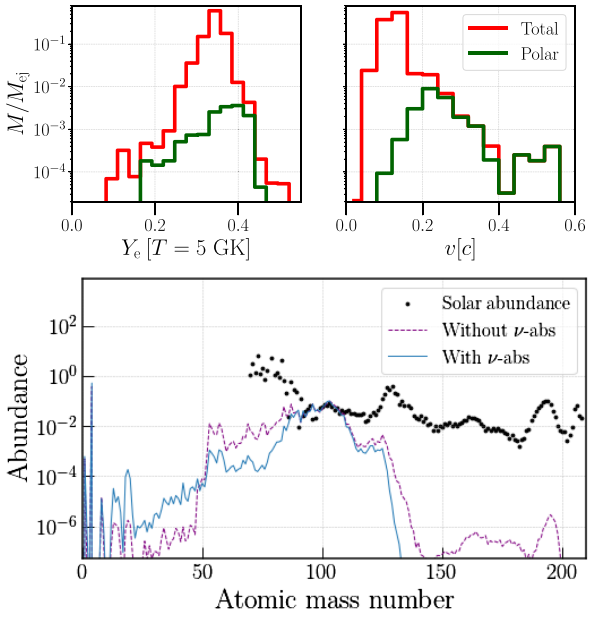

FIG. 5. Top: unbound mass distribution in terms of electron fraction (left; at 5 GK) and asymptotic expansion velocity (right) as sampled by tracer particles, normalized by the total ejected mass, with separate histograms for the polar outflows. Bottom: total final nucleosynthetic abundances at 10^9 s from reaction network calculations for postmerger ejecta, compared to observed solar abundances [77] (arbitrary normalization) with and without including neutrino absorption during r-process nucleosynthesis.

from the self-regulated neutron-rich reservoir of the disk are protonized by absorption of intense neutrino radiation from the remnant (cf. Fig. 2 and Supplemental Material [67]) to a mass-averaged value of $\langle Y_e\rangle \approx 0.3$ at 5 GK.

Nucleosynthesis calculations based on the unbound tracer particles are conducted with the nuclear reaction network SkyNet [78] using 7843 nuclides and 140 000 nuclear reactions with the setup described in Refs. [19] and CS23. They start in nuclear statistical equilibrium at a temperature of $T = 7$ GK and take neutrino irradiation into account using neutrino fluxes directly extracted from our simulation as in Ref. [19]. Final abundances at $t = 10^9$ s are shown in Fig. 5. Elements beyond the second r-process peak ($A \approx 130$) are suppressed.

We compute kilonova light curves based on angular-dependent ejecta mass profiles extracted from the simulation, using the axisymmetric, viewing-angle dependent model of CS23 (see Supplemental Material [67]). The resulting kilonova signal from postmerger ejecta is consistent with observations of GW170817 in the UV and blue bands up to several days (Fig. 6). Underestimation on timescales ≳5 d can be explained by additional "redder" (lanthanide-bearing) components [8] not included here, which can be generated by neutron-richer accretion disk winds upon collapse of the remnant into a BH [9,16,19,32]. The ∼day kilonova is determined by the disk outflows. Fast material from the jet region carries most of the kinetic

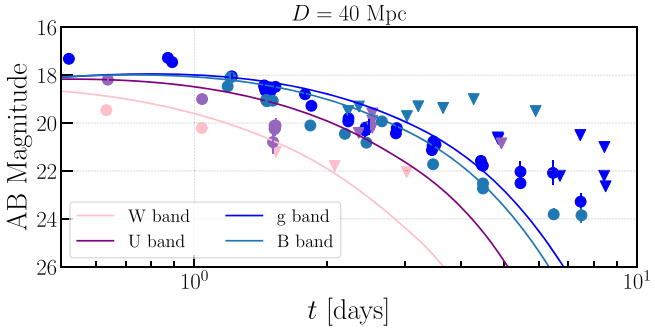

FIG. 6. Kilonova light curves of the $\approx 2 \times 10^{-2} M_\odot$ postmerger ejecta in various UV and blue bands, compared to observed data (dots) and upper limits (triangles) of the GW170817 kilonova [8] and computed for a distance of 40 Mpc with an observer angle of 35° with respect to the rotational axis, as inferred for GW170817 [3,80].

energy but only 10% of the total ejected mass; the latter dominates the signal on a few-hours timescale and can boost the ∼hr UV/blue signal depending on the line of sight (see Supplemental Material [67]). In the direction of the jet, the signal is enhanced by up to 1.5 magnitudes, reaching similar luminosities to the kilonova precursor signal from free neutron decay in fast dynamical ejecta [79] when the boost due to relativistic effects is taken into account (CS23).

Conclusion.—These results provide strong evidence for massive ($\gtrsim 10^{-2} M_\odot$) kilonovae such as GW170817 with early (∼day) blue and late-time (∼week) red emission being dominated by postmerger disk outflows. This provides additional support to the conjecture in Ref. [2] that outflows from accretion disks are the main site of the Galactic r process. We show that binaries consistent with GW170817 and typical of galactic BNS require a remnant lifetime of only ≈50 ms to generate a lanthanide-poor blue kilonova component of $\gtrsim 2 \times 10^{-2} M_\odot$ with expansion velocity $v \approx 0.15c$ and light curves consistent with GW170817. While we find elements of previously proposed mechanisms (magnetized winds [24] and spiral waves [29]), bulk mass ejection here is due to a combination of an incipient magnetic jet ($\sigma \sim 5$–10), associated global magnetic stresses, and the onset of MHD turbulence, which reconfigure the accretion disk, enhancing outflows that quickly dominate the cumulative postmerger ejecta. At $\gtrsim 50$ ms postmerger, the accretion disk with mass of $\approx 0.19 M_\odot$ and accretion rate of $\gtrsim 1 M_\odot$ s^{-1} is in a self-regulated neutrino-cooled state with properties in good agreement with initial conditions of previous work [16,19,32]. We conclude that, upon collapse of the remnant and its neutrino irradiation, lanthanide-bearing outflows of $\gtrsim 0.05 M_\odot$ (∼30% of the remaining disk mass [16–18,27,32,81]) consistent with the red kilonova of GW170817 are generated over the subsequent few hundred milliseconds [16,17,19,32].

The rapid and self-consistent emergence of a weakly magnetized ($\sigma \sim 0.1$), mildly relativistic ($v \lesssim 0.6c$) wind from a merger remnant reported here leads to an ∼hr UV/blue kilonova signal that can be degenerate with the kilonova precursor signal from free neutron decay in the fast tail of dynamical merger ejecta. This novel precursor provides an additional discriminant to distinguish between BNS and NS–black-hole mergers and highlights the importance of early UV and optical follow-up observations of future merger events. The breakout of the jet from the surrounding merger debris observed here may have additional emission signatures, including potential precursors to short gamma-ray bursts [82] (see Supplemental Material [67] with Refs. [83–92] for related work). Upon collapse of the remnant NS, the magnetic jet could "seed" the black hole with magnetic flux and forms a strongly magnetized ($\sigma = L_{\rm EM}/\dot{M} \gg 1$), highly relativistic jet in the absence of stellar winds. This suggests a novel formation mechanism for the central engine of short gamma-ray bursts for remnant lifetimes of $\gtrsim 30$ ms.

The authors thank B. Metzger, D. Desai, G. Ryan, and E. Most for discussions and comments and W. Kastaun for providing visualization tools including the PyCactus package. This research was enabled in part by support provided by SciNet and Compute Canada. The authors gratefully acknowledge the computing time granted by the Resource Allocation Board and provided on the supercomputer Lise and Emmy at NHR@ZIB and NHR@Göttingen as part of the NHR infrastructure. The calculations for this research were conducted with computing resources under the project mvp00022. L. C. acknowledges a CITA National fellowship and acknowledges the support by the Natural Sciences and Engineering Research Council of Canada (NSERC), funding reference No. DIS-2022-568580. D. M. S. acknowledges the support of NSERC, funding reference number No. RGPIN-2019-04684. Research at Perimeter Institute is supported in part by the Government of Canada through the Department of Innovation, Science and Economic Development Canada and by the Province of Ontario through the Ministry of Colleges and Universities.

[1] J. J. Cowan, C. Sneden, J. E. Lawler, A. Aprahamian, M. Wiescher, K. Langanke, G. Martínez-Pinedo, and F.-K. Thielemann, Rev. Mod. Phys. **93**, 015002 (2021).
[2] D. M. Siegel, Nat. Rev. Phys. **4**, 306 (2022).
[3] B. P. Abbott *et al.*, Phys. Rev. Lett. **119**, 161101 (2017).
[4] B. P. Abbott *et al.*, Astrophys. J. Lett. **848**, L12 (2017).
[5] D. A. Coulter *et al.*, Science **358**, 1556 (2017).
[6] M. Soares-Santos *et al.*, Astrophys. J. **848**, L16 (2017).
[7] B. Metzger, G. Martínez-Pinedo, S. Darbha, E. Quataert, A. Arcones, D. Kasen, R. Thomas, P. Nugent, I. Panov, and N. Zinner, Mon. Not. R. Astron. Soc. **406**, 2650 (2010).
[8] V. A. Villar *et al.*, Astrophys. J. **851**, L21 (2017).
[9] D. Kasen, B. Metzger, J. Barnes, E. Quataert, and E. Ramirez-Ruiz, Nature (London) **551**, 80 (2017).
[10] S. J. Smartt *et al.*, Nature (London) **551**, 75 (2017).

[11] E. Pian *et al.*, Nature (London) **551**, 67 (2017).
[12] R. Chornock *et al.*, Astrophys. J. **848**, L19 (2017).
[13] M. Tanaka, D. Kato, G. Gaigalas, and K. Kawaguchi, Mon. Not. R. Astron. Soc. **496**, 1369 (2020).
[14] D. Watson, C. J. Hansen, J. Selsing, A. Koch, D. B. Malesani, A. C. Andersen, J. P. Fynbo, A. Arcones, A. Bauswein, S. Covino *et al.*, Nature (London) **574**, 497 (2019).
[15] M. M. Kasliwal, D. Kasen, R. M. Lau, D. A. Perley, S. Rosswog, E. O. Ofek, K. Hotokezaka, R.-R. Chary, J. Sollerman, A. Goobar *et al.*, Mon. Not. R. Astron. Soc. **510**, L7 (2022).
[16] D. M. Siegel and B. D. Metzger, Phys. Rev. Lett. **119**, 231102 (2017).
[17] R. Fernández, A. Tchekhovskoy, E. Quataert, F. Foucart, and D. Kasen, Mon. Not. R. Astron. Soc. **482**, 3373 (2019).
[18] I. Christie, A. Lalakos, A. Tchekhovskoy, R. Fernández, F. Foucart, E. Quataert, and D. Kasen, Mon. Not. R. Astron. Soc. **490**, 4811 (2019).
[19] X. Li and D. M. Siegel, Phys. Rev. Lett. **126**, 251101 (2021).
[20] D. M. Siegel, Eur. Phys. J. A **55**, 203 (2019).
[21] B. D. Metzger, Living Rev. Relativity **23**, 1 (2020).
[22] D. Radice, S. Bernuzzi, and A. Perego, Annu. Rev. Nucl. Part. Sci. **70**, 95 (2020).
[23] K. Kawaguchi, M. Shibata, and M. Tanaka, Astrophys. J. **865**, L21 (2018).
[24] B. D. Metzger, T. A. Thompson, and E. Quataert, Astrophys. J. **856**, 101 (2018).
[25] R. Ciolfi and J. V. Kalinani, Astrophys. J. Lett. **900**, L35 (2020).
[26] P. Mösta, D. Radice, R. Haas, E. Schnetter, and S. Bernuzzi, Astrophys. J. **901**, L37 (2020).
[27] S. Fujibayashi, S. Wanajo, K. Kiuchi, K. Kyutoku, Y. Sekiguchi, and M. Shibata, Astrophys. J. **901**, 122 (2020).
[28] D. Radice, A. Perego, K. Hotokezaka, S. Bernuzzi, S. A. Fromm, and L. F. Roberts, Astrophys. J. Lett. **869**, L35 (2018).
[29] V. Nedora, S. Bernuzzi, D. Radice, A. Perego, A. Endrizzi, and N. Ortiz, Astrophys. J. **886**, L30 (2019).
[30] S. Fahlman and R. Fernández, Astrophys. J. **869**, L3 (2018).
[31] J. M. Miller, B. R. Ryan, J. C. Dolence, A. Burrows, C. J. Fontes, C. L. Fryer, O. Korobkin, J. Lippuner, M. R. Mumpower, and R. T. Wollaeger, Phys. Rev. D **100**, 023008 (2019).
[32] D. M. Siegel and B. D. Metzger, Astrophys. J. **858**, 52 (2018).
[33] L. Combi and D. M. Siegel, Astrophys. J. **944**, 28 (2023).
[34] L. Baiotti, I. Hawke, P. J. Montero, and L. Rezzolla, Phys. Rev. D **71**, 024035 (2005).
[35] P. Mösta, B. C. Mundim, J. A. Faber, R. Haas, S. C. Noble, T. Bode, F. Löffler, C. D. Ott, C. Reisswig, and E. Schnetter, Classical Quantum Gravity **31**, 015005 (2013).
[36] http://einsteintoolkit.org.
[37] T. Goodale, G. Allen, G. Lanfermann, J. Massó, T. Radke, E. Seidel, and J. Shalf, in *Proceedings of High Performance Computing for Computational Science—VECPAR 2002*, edited by J. M. L. M. Palma, A. A. Sousa, J. Dongarra, and V. Hernández (Springer, Berlin, 2003), pp. 197–227.
[38] E. Schnetter, S. H. Hawley, and I. Hawke, Classical Quantum Gravity **21**, 1465 (2004).
[39] J. Thornburg, Classical Quantum Gravity **21**, 743 (2004).
[40] F. Loffler *et al.*, Classical Quantum Gravity **29**, 115001 (2012).
[41] M. Babiuc-Hamilton, S. R. Brandt, P. Diener, M. Elley, Z. Etienne, G. Ficarra, R. Haas, H. Witek, M. Alcubierre, D. Alic *et al.*, Zenodo (2019), https://zenodo.org/records/3522086.
[42] D. M. Siegel, P. Mösta, D. Desai, and S. Wu, Astrophys. J. **859**, 71 (2018).
[43] D. Radice, F. Galeazzi, J. Lippuner, L. F. Roberts, C. D. Ott, and L. Rezzolla, Mon. Not. R. Astron. Soc. **460**, 3255 (2016).
[44] D. Radice, A. Perego, K. Hotokezaka, S. A. Fromm, S. Bernuzzi, and L. F. Roberts, Astrophys. J. **869**, 130 (2018).
[45] E. Gourgoulhon, P. Grandclement, K. Taniguchi, J.-A. Marck, and S. Bonazzola, Phys. Rev. D **63**, 064029 (2001).
[46] A. Akmal, V. Pandharipande, and D. Ravenhall, Phys. Rev. C **58**, 1804 (1998).
[47] A. S. Schneider, C. Constantinou, B. Muccioli, and M. Prakash, Phys. Rev. C **100**, 025803 (2019).
[48] P. Landry, R. Essick, and K. Chatziioannou, Phys. Rev. D **101**, 123007 (2020).
[49] H. T. Cromartie, E. Fonseca, S. M. Ransom, P. B. Demorest, Z. Arzoumanian, H. Blumer, P. R. Brook, M. E. DeCesar, T. Dolch, J. A. Ellis *et al.*, Nat. Astron. **4**, 72 (2020).
[50] D. Price and S. Rosswog, Science **312**, 719 (2006).
[51] M. Anderson, E. W. Hirschmann, L. Lehner, S. L. Liebling, P. M. Motl, D. Neilsen, C. Palenzuela, and J. E. Tohline, Phys. Rev. Lett. **100**, 191101 (2008).
[52] K. Kiuchi, P. Cerdá-Durán, K. Kyutoku, Y. Sekiguchi, and M. Shibata, Phys. Rev. D **92**, 124034 (2015).
[53] K. Kiuchi, K. Kyutoku, Y. Sekiguchi, and M. Shibata, Phys. Rev. D **97**, 124039 (2018).
[54] W. Kastaun and F. Ohme, Phys. Rev. D **104**, 023001 (2021).
[55] W. Kastaun and F. Galeazzi, Phys. Rev. D **91**, 064027 (2015).
[56] R. Ciolfi, W. Kastaun, B. Giacomazzo, A. Endrizzi, D. M. Siegel, and R. Perna, Phys. Rev. D **95**, 063016 (2017).
[57] W. Kastaun and F. Galeazzi, Phys. Rev. D **91**, 064027 (2015).
[58] S. Fujibayashi, K. Kiuchi, N. Nishimura, Y. Sekiguchi, and M. Shibata, Astrophys. J. **860**, 64 (2018).
[59] M. Chabanov, S. D. Tootle, E. R. Most, and L. Rezzolla, Astrophys. J. Lett. **945**, L14 (2023).
[60] C. Palenzuela, R. Aguilera-Miret, F. Carrasco, R. Ciolfi, J. Kalinani, W. Kastaun, B. Miñano, and D. Viganò, Phys. Rev. D **106**, 023013 (2022).
[61] R. Aguilera-Miret, C. Palenzuela, F. Carrasco, and D. Viganò, Phys. Rev. D **108**, 103001 (2023).
[62] D. Lynden-Bell, Mon. Not. R. Astron. Soc. **279**, 389 (1996).
[63] L. Dessart, C. Ott, A. Burrows, S. Rosswog, and E. Livne, Astrophys. J. **690**, 1681 (2009).
[64] A. Perego, S. Rosswog, R. Cabezon, O. Korobkin, R. Kaeppeli, A. Arcones, and M. Liebendorfer, Mon. Not. R. Astron. Soc. **443**, 3134 (2014).
[65] D. K. Desai, D. M. Siegel, and B. D. Metzger, Astrophys. J. **931**, 104 (2022).
[66] F. Michel, Astrophys. J. **158**, 727 (1969).

[67] See Supplemental Material at http://link.aps.org/supplemental/10.1103/PhysRevLett.131.231402 for more details and figures on the outflow properties and Kilonova model we used. We also present a detailed comparison and discussion of recent related results in the literature.
[68] O. Gottlieb, O. Bromberg, C. B. Singh, and E. Nakar, Mon. Not. R. Astron. Soc. **498**, 3320 (2020).
[69] O. Bromberg and A. Tchekhovskoy, Mon. Not. R. Astron. Soc. **456**, 1739 (2016).
[70] F. Foucart, P. Mösta, T. Ramirez, A. J. Wright, S. Darbha, and D. Kasen, Phys. Rev. D **104**, 123010 (2021).
[71] V. Nedora, D. Radice, S. Bernuzzi, A. Perego, B. Daszuta, A. Endrizzi, A. Prakash, and F. Schianchi, Mon. Not. R. Astron. Soc. **506**, 5908 (2021).
[72] L. Lehner, S. L. Liebling, C. Palenzuela, and P. M. Motl, Phys. Rev. D **94**, 043003 (2016).
[73] D. Radice, S. Bernuzzi, and C. D. Ott, Phys. Rev. D **94**, 064011 (2016).
[74] W. E. East, V. Paschalidis, F. Pretorius, and S. L. Shapiro, Phys. Rev. D **93**, 024011 (2016).
[75] A. M. Beloborodov, Astrophys. J. **588**, 931 (2003).
[76] W.-X. Chen and A. M. Beloborodov, Astrophys. J. **657**, 383 (2007).
[77] M. Arnould, S. Goriely, and K. Takahashi, Phys. Rep. **450**, 97 (2007).
[78] J. Lippuner and L. F. Roberts, Astrophys. J. Suppl. Ser. **233**, 18 (2017).
[79] B. D. Metzger, A. Bauswein, S. Goriely, and D. Kasen, Mon. Not. R. Astron. Soc. **446**, 1115 (2015).
[80] K. P. Mooley, A. T. Deller, O. Gottlieb, E. Nakar, G. Hallinan, S. Bourke, D. A. Frail, A. Horesh, A. Corsi, and K. Hotokezaka, Nature (London) **561**, 355 (2018).
[81] S. De and D. M. Siegel, Astrophys. J. **921**, 94 (2021).
[82] C. Chirenti, S. Dichiara, A. Lien, M. C. Miller, and R. Preece, Nature (London) **613**, 253 (2023).
[83] R. Ciolfi, Mon. Not. R. Astron. Soc. **495**, L66 (2020).
[84] R. Ciolfi, W. Kastaun, J. V. Kalinani, and B. Giacomazzo, Phys. Rev. D **100**, 023005 (2019).
[85] E. R. Most and E. Quataert, Astrophys. J. Lett. **947**, L15 (2023).
[86] S. Curtis, P. Bosch, P. Mösta, D. Radice, S. Bernuzzi, A. Perego, R. Haas, and E. Schnetter, arXiv:2305.07738.
[87] S. Curtis, P. Bosch, P. Mösta, D. Radice, S. Bernuzzi, A. Perego, R. Haas, and E. Schnetter, arXiv:2305.07738.
[88] D. Radice, S. Bernuzzi, A. Perego, and R. Haas, Mon. Not. R. Astron. Soc. **512**, 1499 (2022).
[89] K. Kiuchi, A. Reboul-Salze, M. Shibata, and Y. Sekiguchi, arXiv:2306.15721.
[90] K. Hotokezaka and E. Nakar, Astrophys. J. **891**, 152 (2020).
[91] S. Banerjee, M. Tanaka, K. Kawaguchi, D. Kato, and G. Gaigalas, Astrophys. J. **901**, 29 (2020).
[92] Z. Wu, G. Ricigliano, R. Kashyap, A. Perego, and D. Radice, Mon. Not. R. Astron. Soc. **512**, 328 (2022).